EUROPEAN ORGANIZATION FOR NUCLEAR RESEARCH

CERN-EP/84-21
24 February 1984

MARS-2 : A "CURRENT SENSITIVE" LIQUID ARGON CALORIMETER

INFN Pisa[1]-Serpukhov[2] Collaboration

C. Cerri[1,*)], S.P. Denisov[2], G. Gennaro[1], R.N. Krasnokutsky[2], A.A. Lebedev[2], S.A. Medved[2], V.S. Mikhailov[2], N.I. Naumov[2], M. Ragadini[1], E.A. Rasuvaev[2], F. Sergiampietri[1], R.S. Shuvalov[2], G. Spandre[1] and D.A. Stoyanova[2]

ABSTRACT

The performances of a liquid argon calorimeter with wide gaps (2.8 cm) operating in current sensitive mode have been studied with 6.6 ÷ 36 GeV electron and 40 GeV pion beams at the IHEP accelerator.

The good uniformity in charge collection efficiency obtained with this unusual mode has led to a reduction of sampling fluctuations to values of $\sigma_S/E = 0.04/\sqrt{E}$.

Spatial and angular resolutions have been measured as well. The equivalent noise energy was 82 MeV rms for the whole detector.

(Submitted to Nuclear Instruments and Methods in Physics Research)

1) Istituto Nazionale di Fisica Nucleare, Sezione di Pisa, Italy.
2) Institute for High Energy Physics, Serpukhov, USSR.
*) Now at CERN, Geneva, Switzerland.

1. Introduction

As pointed out in a previous paper[1], the main contributions to energy resolution of electromagnetic showers developing in liquid argon calorimeters come from: a) fluctuations in energy sharing between passive (electrodes) and active (liquid argon) absorbers; b) fluctuations of the output signal due to a non uniform charge collection efficiency along the liquid argon gap (position dependence).

An obvious way to reduce the first kind of fluctuations is to minimize the fraction of the passive material. For the second kind of fluctuations improvements can be achieved utilizing facts such as the drifting charge attenuation[2] (due to the attachment of electronegative impurities) or the integration of the signal for short times if compared to the total drift time[3]. Both these methods allow to keep the collection efficiency rather uniform although they reduce the output signal.

Conditions under which the equivalent noise charge (*ENC*) from the associated electronics results proportionally reduced can be found as for the case of the MARS-2 calorimeter structure described in this paper.

The working principles of this calorimeter will be presented in section 2. In section 3 the geometry, the electrical connections and other experimental conditions will be described. Results of tests with electron and pion beams of different energies are reported in section 4.

2. Working principles of the current sensitive structure

A liquid argon calorimeter with wide signal plane-ground plane gap, ~10 times larger than the traditionally used, has been constructed. For such a structure the dependence of the collection efficiency on the track position along the gap turns out to be quite negligeable if the current signal is integrated just over the initial fraction (T_i) of the total drift time (T_d).

A simplified model of sampling fluctuations for electromagnetic showers[4] has given indications about the dependence of energy resolution (σ_S) on the main parameters of sampling calorimeters, particularly on the fraction of energy released in liquid argon (α), on the attenuation length (λ) and on the relative integration time ($\tau = T_i/T_d$).

Calculations carried on the basis of such a model have resulted in the following expression for σ_S/E:

$$\frac{\sigma_S}{E} \propto \eta(\alpha, \lambda', \tau) \cdot \sqrt{\frac{\Delta_c}{E}} \tag{1}$$

Δ_c being the energy loss per elementary cell, $\lambda' = \lambda/D$, where D is the gap width.

Although an increased gap reflects into a greater Δ_c value, a resulting significant reduction of the η factor is obtained in the region of relatively high α values if T_i or λ are short enough. Such behaviour has been also confirmed by a Montecarlo simulation[5].

Reduced sampling fluctuations for $\tau \ll 1$ derive from the fact that the detector is now "sensitive" only to the initial current and hence the collection efficiency becomes rather uniform along the gap.

Of course this uniformity in efficiency is payed by a reduction of the output signal. Nevertheless it can be demonstrated that the S/N ratio in the case of wide gap with integration time $T_i = T_d/n$ is nearly equal to that one obtained when the same volume is covered by n gaps and with integration over the same time (fig. 1).

Indeed, by supposing an optimum matching (via transformer) between the detector capacitance and the amplifier input capacitance[6] we obtain for the two structures of fig. 1:

$$\frac{(ENC)_W}{(ENC)_M} = \frac{1}{n} . \tag{2}$$

In the general case when the attenuation length due to e.n. impurities is λ, the charge signal at time t ($0 \leq t \leq T_d$) is for the two cases:

$$Q_W(t) = Q_o \frac{\lambda}{D}\left[(1-\lambda/D)(1-exp(-tD/T_d\lambda)) + \frac{t}{T_d} exp(-tD/T_d\lambda)\right] \tag{3}$$

$$Q_M(t) = Q_o n \frac{\lambda}{D}\left[(1-n\lambda/D)(1-exp(-tD/T_d\lambda)) + n\frac{t}{T_d} exp(-tD/T_d\lambda)\right]. \tag{4}$$

By evaluating both the expressions at $t = T_d/n$, we have for the ratio $R = (S/N)_W / (S/N)_M$:

$$(5) \qquad R = \frac{1}{n}\left[1 + \frac{(n-1)(1-exp(-D/n\lambda))}{(1-n\lambda/D)(1-exp(-D/n\lambda) + exp(-D/n\lambda)}\right]$$

(for $\lambda \to \infty$, $R \to 2-1/n$).

It must be noted that it is always $R > 1$.

3. MARS-2

The electrode system of the MARS-2 calorimeter is shown schematically in fig. 2. The calorimeter is constituted by a stack of 45 modules (bigaps). Each bigap comprises a 3 mm thick aluminium ground plane, a 28 mm liquid argon gap, a 3 mm thick aluminium signal plane, a second 28 mm liquid argon gap and another 3 mm aluminium ground plane.

Signal and ground planes are hexagonally shaped to contain a circle of 700 mm in diameter. The signal planes are segmented in 7 strips, 100 mm wide and 1 mm apart. Each bigap has the signal strips oriented sequentially at 0° (U), 120° (V), 240° (W) with respect to the vertical direction. The calorimeter results to be constituted by 3 interleaved chambers each one with a different orientation of its strips. In each chamber strips at the same transverse position are five by five electrically connected together to form three longitudinal blocks. The total number of independent channels, so obtained, is 63. The signal from each channel feeds an electronic chain via a decoupling capacitor (made of a metallized kapton film and soldered on the electrodes), a 50 Ω cable and a low voltage feedthrough.

The main parameters of the detector are listed in table 1.

The detector was filled with industrial liquid argon whose oxigen contamination was nearly 3 ppM. The cryogenic system and the electronics for the signal analysis were the same used for the MARS-1 detector and are described in detail in ref. 1. The integration time for the current signal was fixed at 1/20 of the total drift time T_d. This was performed by reducing the integration time constant of the shaping amplifier until the maximum of the shaped signal occurred at $T_i = T_d / 20$ (corresponding to the total drift time in MARS-1).

In this electrode geometry the stray capacitance between adjacent strips is of the order of 1/3 of the capacitance between a strip and ground. This means that the charge signal on one strip (S) induces a cross-talk

signal (X) in the neighbouring ones. The measured ratio between X and S at their maximum is ≅ 0.04. The shape of X is mainly determined by the first derivative of S as it can be seen in fig. 3. Using this fact, X/S was reduced at a level ≅ 0.01 by gating the ADC around the maximum of S which corresponds to the zero-crossing of X.

Each channel was calibrated individually by injecting known charges to span all the dynamic range of the amplifiers. Gain and noise levels were continuously monitored during data taking, by registering events out of the beam bursts.

The average equivalent noise energy (ENE) was for each channel ≅ 11 MeV and for the whole detector ≅ 82 MeV.

4. Results

Data have been taken with 6.6, 11.9, 23.0, 36.0 GeV/c electrons and 40 GeV/c negative pions and muons at the Serpukhov IHEP accelerator. The beam layout was similar to that one used to test the MARS-1 calorimeter. The vacuum pipe has been prolonged along the beam line up to the detector entrance. This led to an improvement in the usual magnetic analysis of beam momentum. The residual spread in momentum measurement was of the order of 0.5 % due to the multiple scattering on unavoidable material (scintillation counters, vacuum windows, ...) and to the MWPC wire spacing. This spread has been estimated from the difference between reconstructed and measured beam particle position in the direction normal to the bending plane. Precise evaluations of this mesurements are reported in table 2.

The full beam pulse height distributions are shown in fig. 4.

4.1. Electrons

Pulse height spectra corrected for beam momentum spread are shown, for all the electron energies, in fig. 5 (if not otherwise stated data refer to a field strength of 0.9 KV/cm). The peaks in the energy spectra have been fitted to Gaussian functions whose means and standard deviations have been used to estimate the energy resolution.

The overall energy resolutions, noise and momentum spreads together with the estimated sampling fluctuations, are presented in table 2. The energy dependence of the intrinsic detector resolution is interpreted by

(see fig. 6a):

$$\frac{\sigma_D}{E} = \sqrt{\left(\frac{\sigma_N}{E}\right)^2 + \left(\frac{k}{\sqrt{E}}\right)^2} \tag{6}$$

E being the energy (in GeV) of the incident electrons, σ_N = 0.082 GeV the rms width of the noise distribution and k = 0.04 $GeV^{0.5}$ the rms width of sampling fluctuations at 1 GeV. In the energy region where the electronic noise is negligeable σ_D/E reduces to :

$$\frac{\sigma_D}{E} \cong \frac{\sigma_S}{E} = \frac{0.04}{\sqrt{E}} \qquad \text{(with } E \text{ in GeV)}. \tag{7}$$

A study of the correlation in energy depositions among the three chambers has been developed too, analogously to what has been done for the previous calorimeter (ref. 1). In the hypothesis of energy fluctuations only due to the sharing of energy among aluminium, chamber U, V and W the theoretical estimation of the correlation coefficient (see appendix), when the average fraction of energy released in liquid argon is α, is:

$$\rho_{TH} = -\frac{\alpha}{3-\alpha} = -0.36 \qquad \text{(for } \alpha = 0.787). \tag{8}$$

By taking into account at the different energies the resolutions of the single chambers and of their differences, these latter not affected by beam momentum spread contributions, an average value of ρ_{EXP} = -0.30 has been derived. This result, in good agreement with ρ_{TH}, confirms that fluctuations due to a non uniform efficiency along the gap and characterized by a zero correlation factor between the chambers have been considerably reduced by the initial current operation mode as explained in section 2.

The dependence of pulse height on the electric field strength has been measured in the range 0.3 ÷ 1.0 KV/cm with 36 GeV electrons. A linear behaviour has been found, as it was expected at such low fields (fig. 7a). The relative energy resolution is anyway nearly constant in this range (fig. 7b).

Space and angular resolutions for e.m. showers have been also measured at the four energies.

The method adopted to find position and angle of each shower axis, based on the determination of the transverse profiles for each longitudinal

block of the calorimeter, has been exhaustively described in ref. 1. The profiles, which are the transverse charge distributions in each block normalized to the total charge in that block, are fitted to the expression:

$$f(x) = \begin{cases} \dfrac{A_1}{2\sqrt{A_2 \cdot |x|}} \exp(-\sqrt{|x|/A_2}) & \text{for } |x| > \xi \\ \dfrac{A_1}{2\sqrt{A_2 \cdot \xi}} \exp(-\sqrt{\xi/A_2}) & \text{for } |x| \leq \xi \end{cases} \tag{9}$$

with A_1 = 0.75 mm, A_2 = 9.66 mm and ξ = 4.78 mm.

Data at 11.9, 23.0 and 36.0 GeV are shown in fig. 8.

The distributions of the differences in position and angle as measured by the MWPC's and as reconstructed with the calorimeter are shown for 23 GeV e^- in fig. 9. The dependences of the spatial and angular resolutions for one chamber (*V*) on incident energy are shown in fig. 6b and 6c and they can be expressed in the following form:

$$\sigma(x) = \sqrt{\left(\frac{31.4}{E}\right)^2 + \left(\frac{21.6}{\sqrt{E}}\right)^2} \text{ mm},$$

$$\sigma(\theta) = \sqrt{\left(\frac{58.0}{E}\right)^2 + \left(\frac{41.5}{\sqrt{E}}\right)^2} \text{ mrads}, \tag{10}$$

the first term in both expressions being related to the noise contributions and the second one to the statistical fluctuations of the shower.

Indeed, both the resolutions depend on the transverse position of the incident electron. The expressions in (10) are obtained by averaging over all these positions. Fig. 10 shows the spatial resolution at different impact points inside the central strip.

The possibility to distinguish (and to reject) hadrons from electrons has been also studied utilizing as only discriminating parameter the rms width of the transverse energy deposition (σ_t). In fig. 11 the σ_t distributions for hadrons and electrons are shown. By accepting events with 60 mm $\leq \sigma_t \leq$ 93 mm, the rejection factor obtained is $< 4 \cdot 10^{-2}$ with an efficiency for e.m. showers of $\cong$ 99 %.

4.2. Muons

In fig. 12 the pulse height distribution obtained with 40 GeV/c μ^- is reported. The MARS-2 capability to detect minimum ionizing particles results from the comparison of the noise spectrum, drawn in the same figure, with the muon spectrum.

To check the internal consistency of data it is interesting to compare the electron peak at one energy with the muon peak. A correct way to calculate the two peak positions can be the following:

- for muons

$$E_\mu = \left.\frac{dE}{dx}\right|_{40\ GeV} \cdot \ell(LA) = 3.23\ MeV/cm \cdot 252\ cm = 0.81\ GeV$$

where $\ell(LA)$ is the total liquid argon thickness;

- for electrons

$$E_e = \alpha(\varepsilon) \cdot E_i = 0.787 \cdot 23.0\ GeV = 18.14\ GeV$$

where α is calculated at the average critical energy ε and E_i the incident electron energy.

The calculated ratio $R_c = E_e / E_\mu$ results in this case 22.3 to be compared with the experimental value R_{exp} = 22.0.

This good agreement let to exclude visible transition effects[7] connected with the amplification or the attenuation of the shower population when crossing boundaries between aluminium and liquid argon layers. This could be explained with the small difference in critical energy between the two materials (ε_{LA} = 34.5 MeV and ε_{Al} = 47.0 MeV) and/or the small thickness of the electrodes.

5. Conclusions

As the results of the test performed on the MARS-2 calorimeter has stated, the wide gap structure working in the current sensitive mode is equivalent, as it concerns energy resolution, to the fine grain structure of the previously constructed calorimeter based on the traditional charge integrating mode.

The uniformity in collection efficiency obtained with this method has led to a reduction of fluctuations in the output signal which affect the intrinsic energy resolution of the detector.

Satisfacting results also in terms of spatial and angular resolution have been achieved although the transverse and longitudinal definition of the shower development was not so detailed as for MARS-1. Moreover the low noise level allows to detect and identify minimum ionizing particles and, joined to the low capacitance of each channel, opens the possibility to extract fast signals for triggering.

Indeed, the high performances of this calorimeter, the possibility to work with industrial liquid argon and with low electric field, to construct and assemble the structure easely and in short time, have brought to adopt this solution for the big liquid argon spectrometer (BARS) that is going to be used in experiments with tagged neutrino beams at the Serpukhov accelerator.

We whish to thank L. Corucci, N. Filimonov, R. Franceschini and V. V. Volkov who collaborated during the assembling of the detector. We also whish to thank Yu. M. Antipov, V. A. Bezzubov, Yu. P. Gorin, A. I. Petrukhin and A. P. Soldatov who helped us during the measurements and N. A. Galyaev, V. A. Pichugin and V. N. Zapolsky for the beam tuning. We would like to thank the IHEP (Serpukhov) and the INFN (Pisa) directorates for their support.

Appendix. Estimation of the correlation coefficient ρ_{TH}.

Let be:

E_i = e^- incident energy = constant

E_a = energy deposited in liquid argon

E_u, E_v, E_w = energies deposited in U, V, W interleaved chambers

$\alpha = E_a / E_i$.

It is:

(1A) $$E_a = E_u + E_v + E_w$$

(2A) $$\sigma_a^2 = \sigma_u^2 + \sigma_v^2 + \sigma_w^2 + 2\rho_{uv}\sigma_u\sigma_v + 2\rho_{vw}\sigma_v\sigma_w + 2\rho_{wu}\sigma_w\sigma_u$$

In first approximation it can be considered:

$$\rho_{uv} \cong \rho_{vw} \cong \rho_{wu} = \rho_{TH}$$

$$\sigma_u \cong \sigma_v \cong \sigma_w = \sigma_c$$

With such conditions expression (2A) becomes:

(3A) $\sigma_a^2 = 3\sigma_c^2(1 + 2\rho_{TH})$, hence:

(4A) $$\rho_{TH} = \frac{1}{2}\left(\frac{\sigma_a^2}{3\sigma_c^2} - 1\right)$$

By supposing the total energy E_i deposited in N elementary losses E_e, i. e. $E_i = NE_e$, it is :

(5A)
$$n_a = \alpha N \quad \text{average number of elementary losses in liquid argon,}$$
$$n_u \cong n_v \cong n_w \cong n_c = \alpha N/3 \quad \text{average number of elementary losses in each chamber.}$$

Then σ_c and σ_a can be expressed as:

(6A)
$$\sigma_a^2 = \alpha(1-\alpha)N$$
$$\sigma_c^2 = \frac{\alpha}{3}(1-\frac{\alpha}{3})N$$

By replacing expressions (6A) in (4A) we obtain:

(7A) $$\rho_{TH} = -\frac{\alpha}{3-\alpha} .$$

Analogously it can be shown that in the general case of m interleaved chambers ρ_{TH} becomes:

$$\rho_{TH} = -\frac{\alpha}{m-\alpha} .$$

References

1. - C. Cerri et al., N.I.M. 214 (1983) 217.

2. - B. M. Ovchinnikov, Preprint INR, P-0085, Moscow, 1978.

3. - V. Radeka, IEEE Trans. Nucl. Sci., NS-24, No.1 (1977) 293.

4. - F. Sergiampietri et al., "Analytical calculations of sampling fluctuations", to be published.

5. - B. E. Stern, preprints INR 11-0081/82 M.(1978).

6. - W. J. Willis and V. Radeka, N.I.M. 120 (1974) 221.

7. - R. F. Cristy and S. Kusaka, Phys. Rev. 59 (1941) 414; K. Pinkau, Phys. Rev. 139 (1965) 1548; C. J. Crannel, Phys. Rev. 182 (1969) 1441.

Table 1

Characteristics and parameters of cell and of detector

D_a,	gap width (LA)	28	cm
D_s,	signal electrode thickness (Al)	3	mm
D_g,	ground electrode thickness (Al)	3	mm
ρ,	average density	1.58	g/cm^3
X_o,	average radiation length	13.0	cm
λ,	average absorption length	69.6	cm
ε,	average critical energy	37.5	MeV
R_M,	average Molière unit	7.26	cm
D_c,	elementary cell	32.5	mm
		7.9	MeV *)
		0.25	X_o
α	$= dE(LA)/\, dE(LA) + dE(Al)$	0.787	†)
L,	total length	2925	mm
D,	useful section diameter	700	mm
W,	strip width	100	mm
N_s,	number of signal planes	45	
N_t,	number of strips per plane	7	
N_c,	number of coordinates	3 at 120°	
N_l,	number of longitudinal blocks per coordinate	3	
N_{ch},	total number of channels	3×3×7 = 63	
C_T,	total detector capacitance	38	nF

*) For minimum ionizing particles.

†) For electrons at the average critical energy.

Table 2

Width for the U, V, W chambers and for the whole detector for 6.6, 11.9, 23.0 and 36.0 GeV electrons.

	6.6 GeV				11.9 GeV			
	U	V	W	TOT	U	V	W	TOT
$<E>$, GeV	2.05	2.18	2.36	6.62	3.77	3.96	4.12	11.87
σ_T, GeV	0.132	0.132	0.137	0.138	0.174	0.161	0.171	0.170
σ_B/E, %	0.69	0.69	0.69	0.69	0.61	0.61	0.61	0.61
$<\sigma_N>$, GeV	0.046	0.041	0.043	0.082	0.046	0.041	0.043	0.082
σ_D, GeV	0.131	0.131	0.136	0.132	0.172	0.159	0.169	0.154
σ_D/E, %	6.4	6.0	5.8	2.0	4.6	4.0	4.1	1.3
σ_S, GeV	0.123	0.125	0.129	0.101	0.166	0.154	0.164	0.130
σ_S/E, %	6.0	5.7	5.5	1.5	4.4	3.9	4.0	1.1
	23.0 GeV				36.0 GeV			
	U	V	W	TOT	U	V	W	TOT
$<E>$, GeV	7.37	7.72	7.92	23.05	11.74	12.06	12.18	36.03
σ_T, GeV	0.254	0.229	0.232	0.243	0.295	0.292	0.295	0.319
σ_B/E, %	0.53	0.53	0.53	0.53	0.47	0.47	0.47	0.47
$<\sigma_N>$, GeV	0.046	0.041	0.043	0.082	0.046	0.041	0.043	0.082
σ_D, GeV	0.251	0.225	0.228	0.210	0.290	0.287	0.290	0.271
σ_D/E, %	3.4	2.9	2.9	0.9	2.5	2.4	2.4	0.8
σ_S, GeV	0.247	0.222	0.224	0.194	0.286	0.284	0.286	0.259
σ_S/E, %	3.4	2.9	2.8	0.8	2.4	2.4	2.4	0.7

Figure captions

Fig. 1 - Wide gap and multigap structures.

Fig. 2 - MARS-2 electrode system. (During the test, for each plane, only the seven central strips were connected to the read-out electronics).

Fig. 3 - Charge signal in one strip (S) and cross-talk signal (X) in the neighbouring one. Horizontal scale: 200 ns/cm; vertical scales for S 1 volt/cm, for X 100 mV/cm.

Fig. 4 - Full beam pulse height distributions as seen by MARS-2 for 6.6, 11.9, 23.0, 36.0 GeV e^- and for 40 Gev π^-.

Fig. 5 - Pulse height spectra corrected for beam momentum spread at the four electron energies.

Fig. 6 - Energy dependence of the a)intrinsic energy resolution (•), sampling fluctuations (o), b)spatial resolution, c)angular resolution. The dashed lines are obtained quadratically unfolding the noise contribution and they represent the resolutions in energy regions where noise is negligeable.

Fig. 7 - Pulse height (•) and relative energy resolution (o) dependencies on the applied electric field for 36.0 GeV e^-.

Fig. 8 - Transversal profiles at 11.9 (▲), 23.0 (●), 36.0 (■) GeV e^- compared with one obtained in the MARS-1 calorimeter (26.6 GeV e^-, o). The fit refers to 23.0 GeV e^-.

Fig. 9 - Distributions for 23.0 GeV e^- of $\Delta\theta V_{ab} = \theta V_a - \theta V_b$ (a), $\Delta V_{ab} = V_a - V_b$ (b). The suffix a refers to the measured incident electron impact coordinate in V plane and b refers to the recontructed one from the calorimeter information.

Fig.10 - Dependence of the spatial resolution on the beam impact position inside the central strip. The solid line refers to the V coordinate; the dashed line refers to the W coordinate. The resolution improves towards the edges of the strip because in these positions more than one strip is occupied by a relevant fraction of the shower.

Fig.11 - Rms width of the transverse energy deposition for electrons and hadrons.

Fig.12 - Pulse height distribution for 40 GeV/c muons. For comparison it is also shown the noise spectrum (shaded histogram).

Wide gap structure

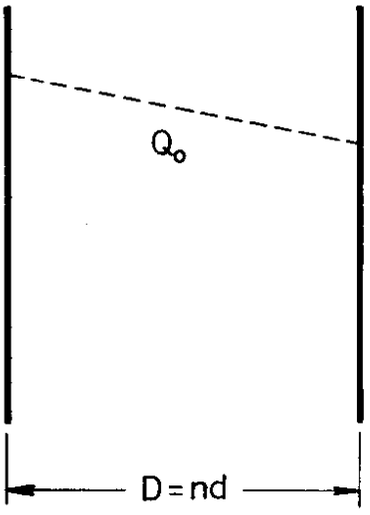

$C_W = C/n$

Multigap structure

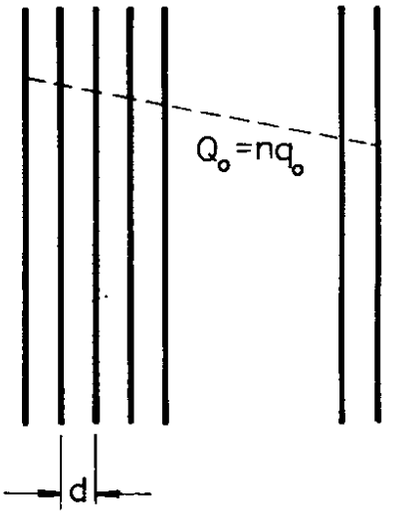

$C_M = nC$

With optimum matching transformer:

$(ENC)_W = k\sqrt{C_W}$

$(ENC)_M = k\sqrt{C_M}$

Fig. 1

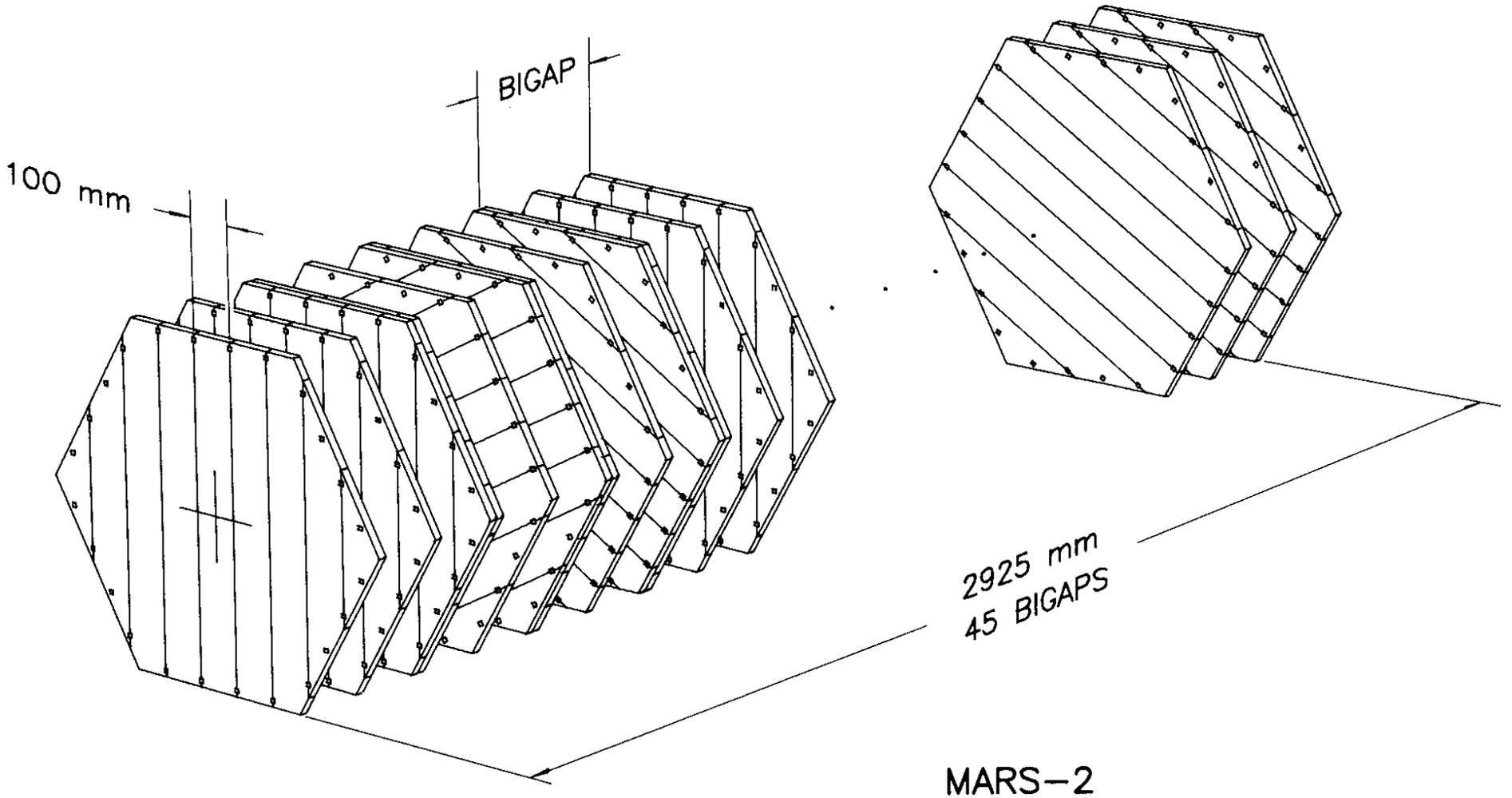

Fig. 2

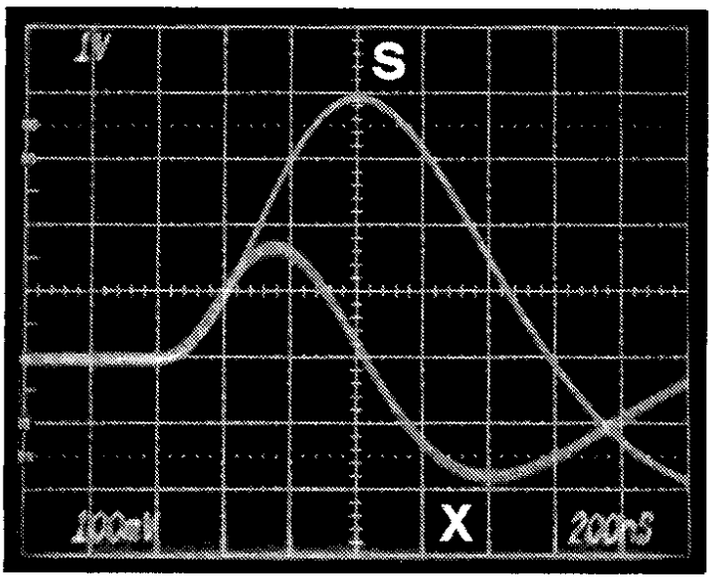

Fig. 3

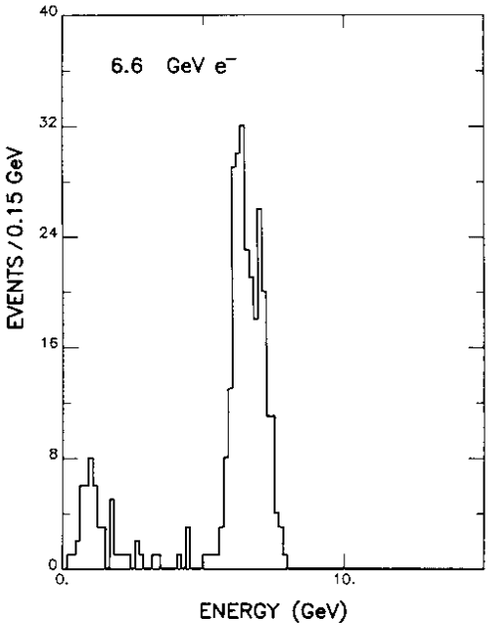
6.6 GeV e⁻
EVENTS / 0.15 GeV
ENERGY (GeV)

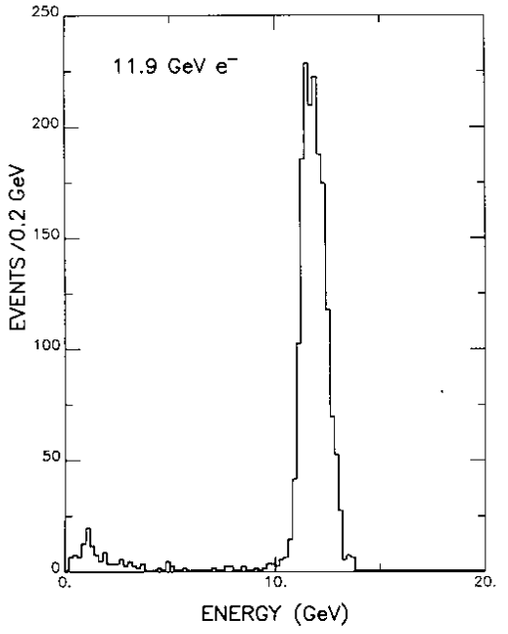
11.9 GeV e⁻
EVENTS / 0.2 GeV
ENERGY (GeV)

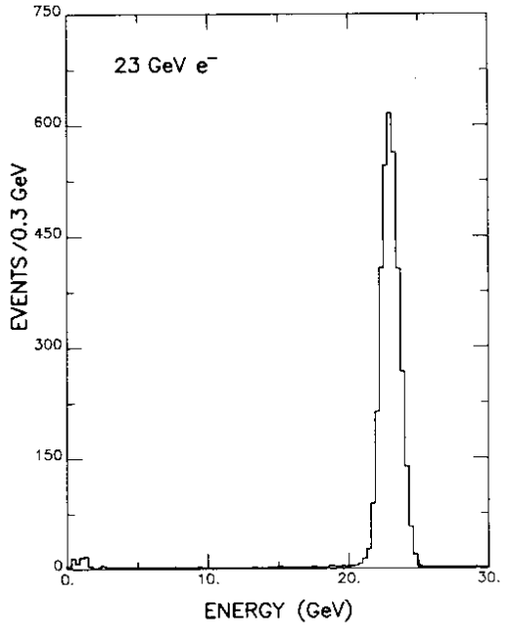
23 GeV e⁻
EVENTS / 0.3 GeV
ENERGY (GeV)

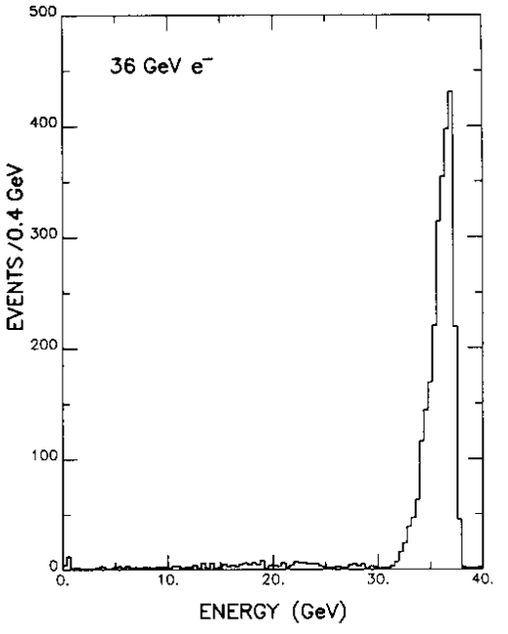
36 GeV e⁻
EVENTS / 0.4 GeV
ENERGY (GeV)

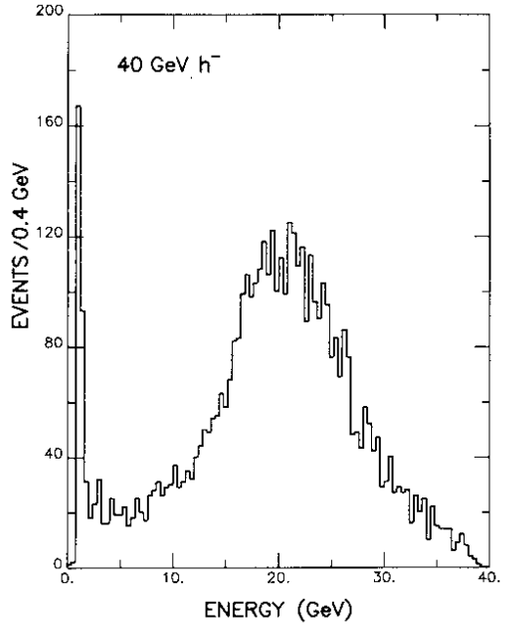
40 GeV h⁻
EVENTS / 0.4 GeV
ENERGY (GeV)

Fig. 4

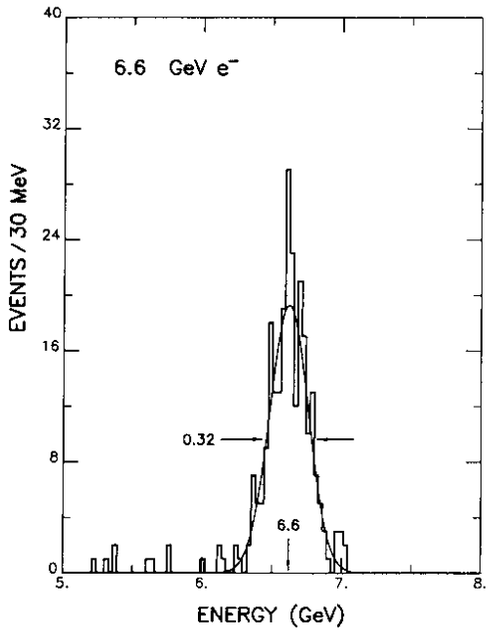
6.6 GeV e⁻
EVENTS / 30 MeV
0.32
6.6
ENERGY (GeV)

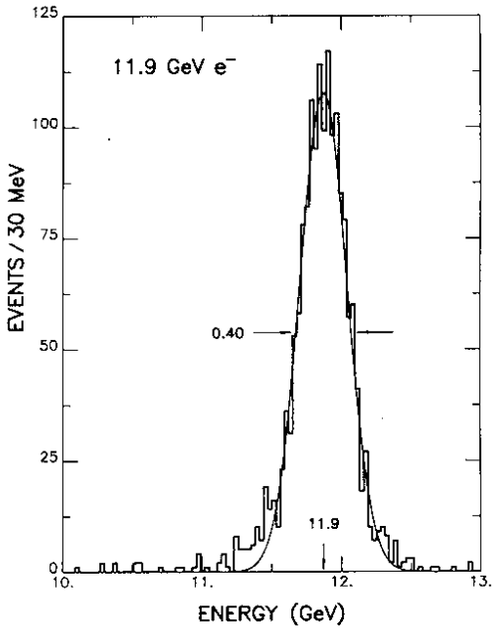
11.9 GeV e⁻
EVENTS / 30 MeV
0.40
11.9
ENERGY (GeV)

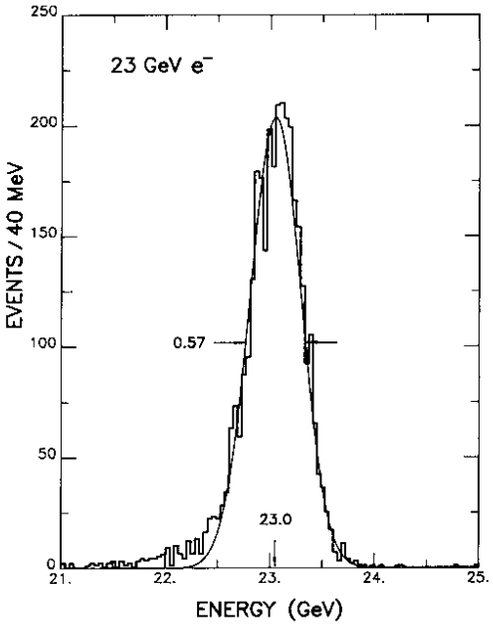
23 GeV e⁻
EVENTS / 40 MeV
0.57
23.0
ENERGY (GeV)

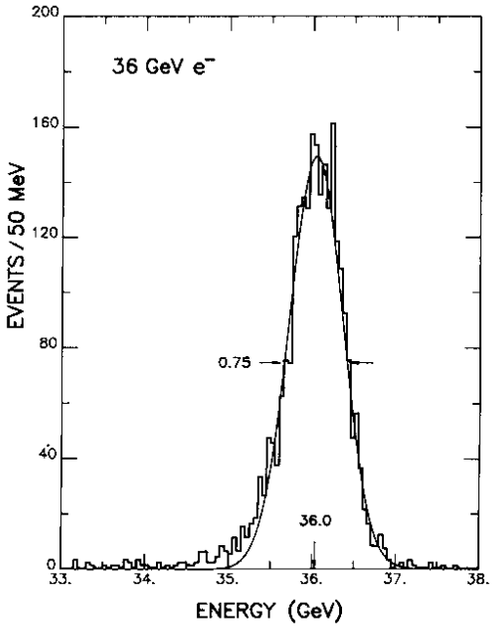
36 GeV e⁻
EVENTS / 50 MeV
0.75
36.0
ENERGY (GeV)

Fig. 5

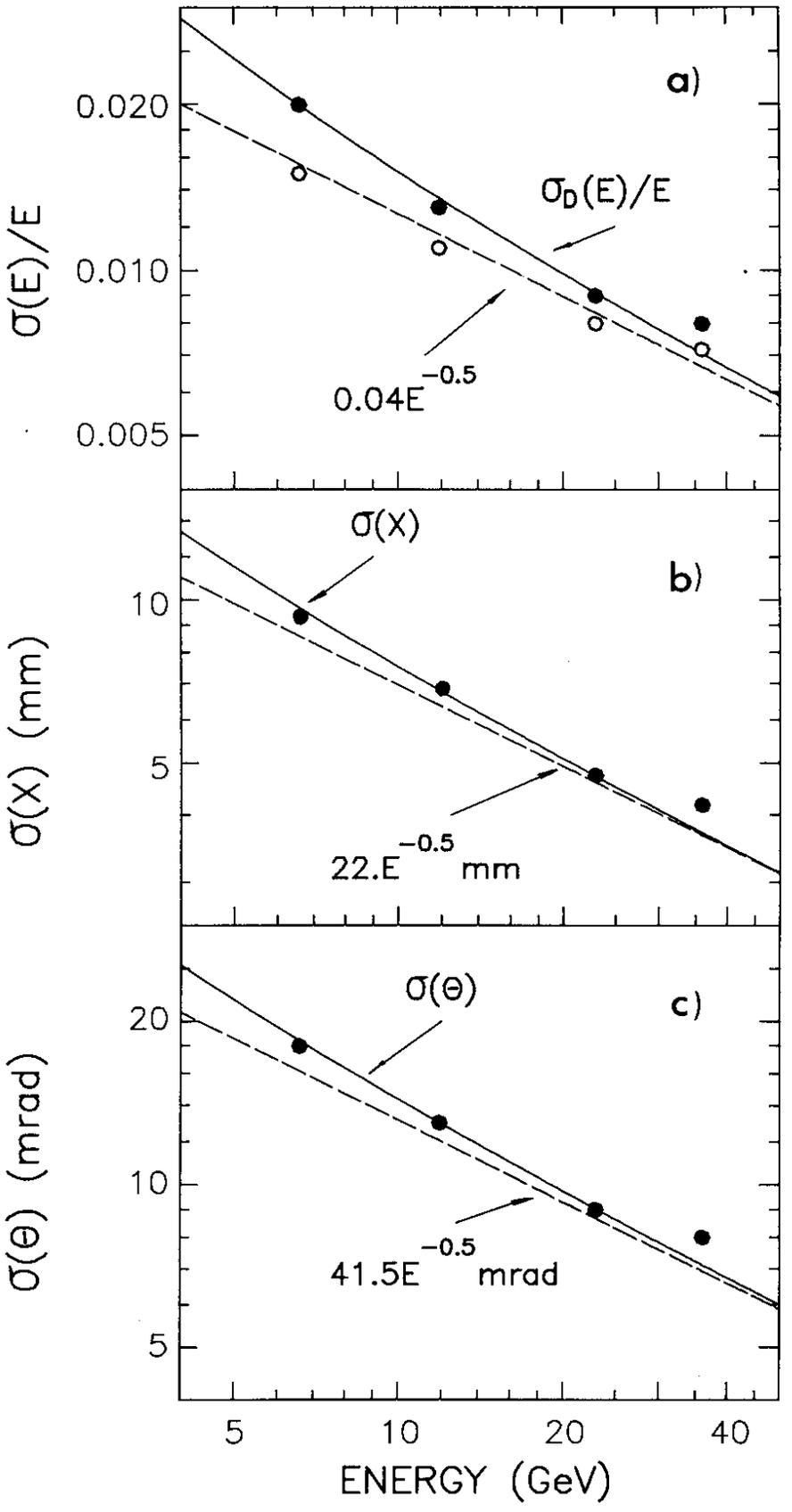
a)
0.020
0.010
0.005
σ(E)/E
σD(E)/E
0.04E−0.5
b)
σ(X)
10
5
σ(X) (mm)
22.E−0.5 mm
c)
σ(θ)
20
10
5
σ(θ) (mrad)
41.5E−0.5 mrad
5
10
20
40
ENERGY (GeV)

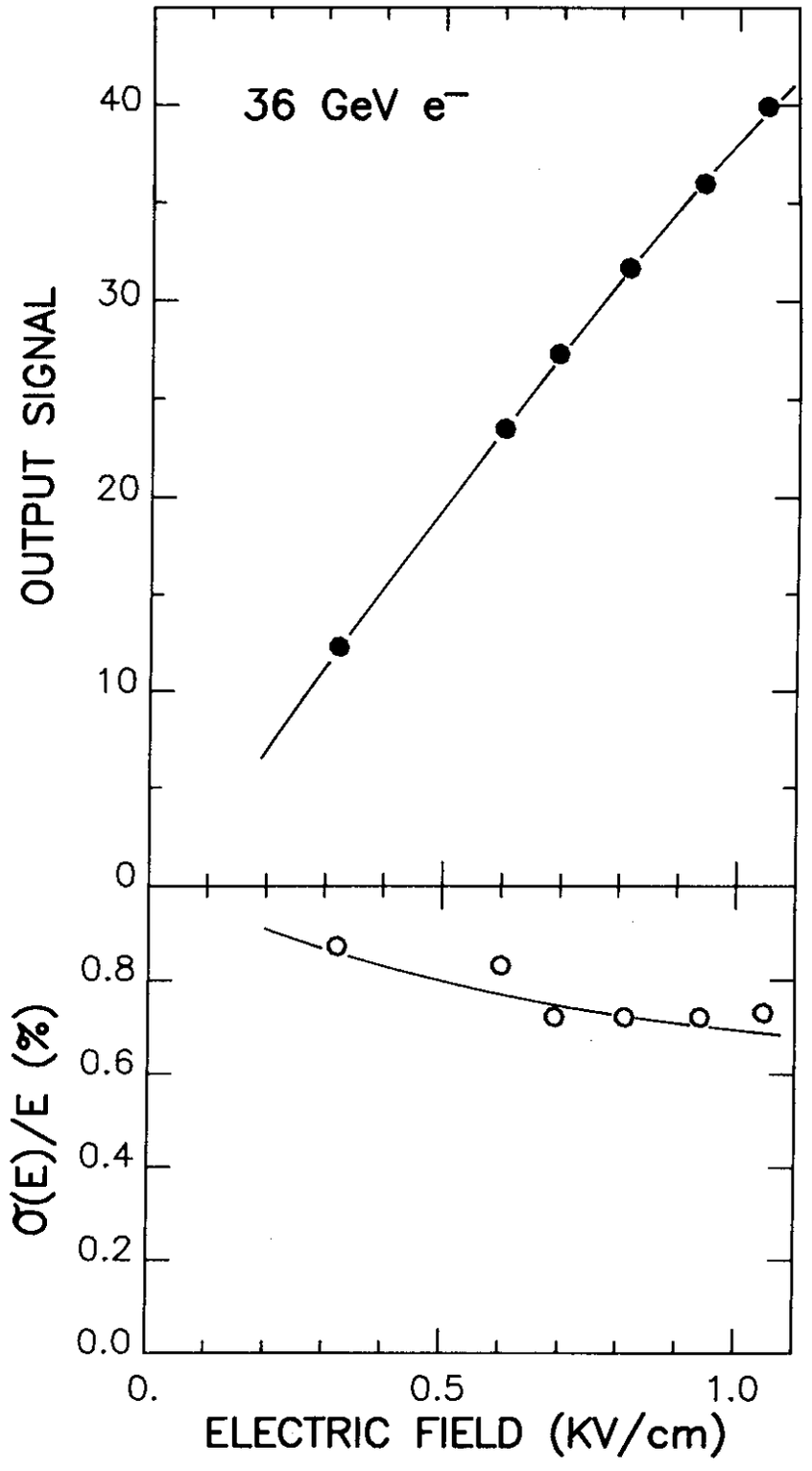
36 GeV e⁻
OUTPUT SIGNAL
40
30
20
10
0
σ(E)/E (%)
0.8
0.6
0.4
0.2
0.0
0.
0.5
1.0
ELECTRIC FIELD (KV/cm)

Fig. 7

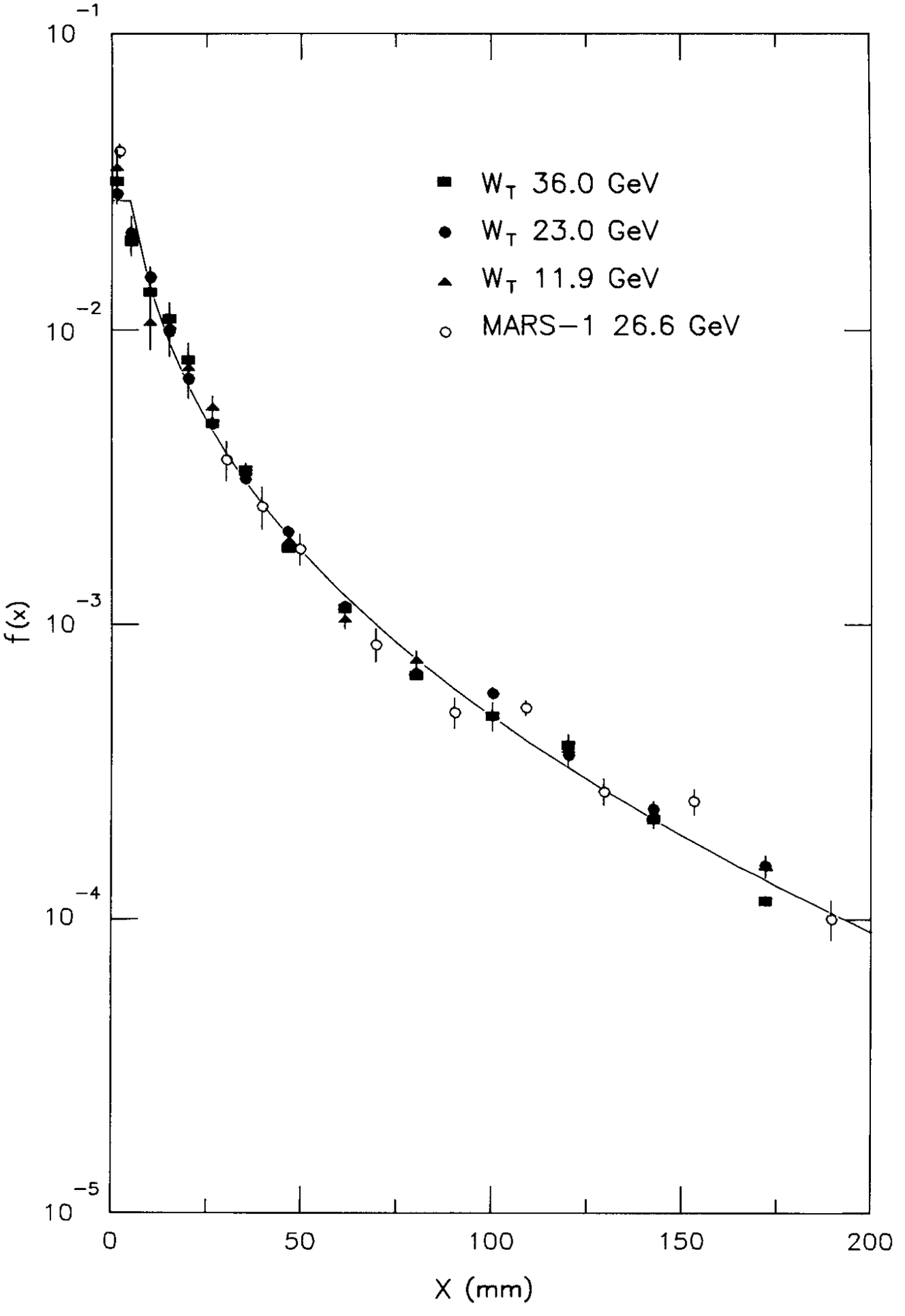
W_T 36.0 GeV
W_T 23.0 GeV
W_T 11.9 GeV
MARS−1 26.6 GeV
f(x)
X (mm)
10^{-1}
10^{-2}
10^{-3}
10^{-4}
10^{-5}
0
50
100
150
200

Fig. 8

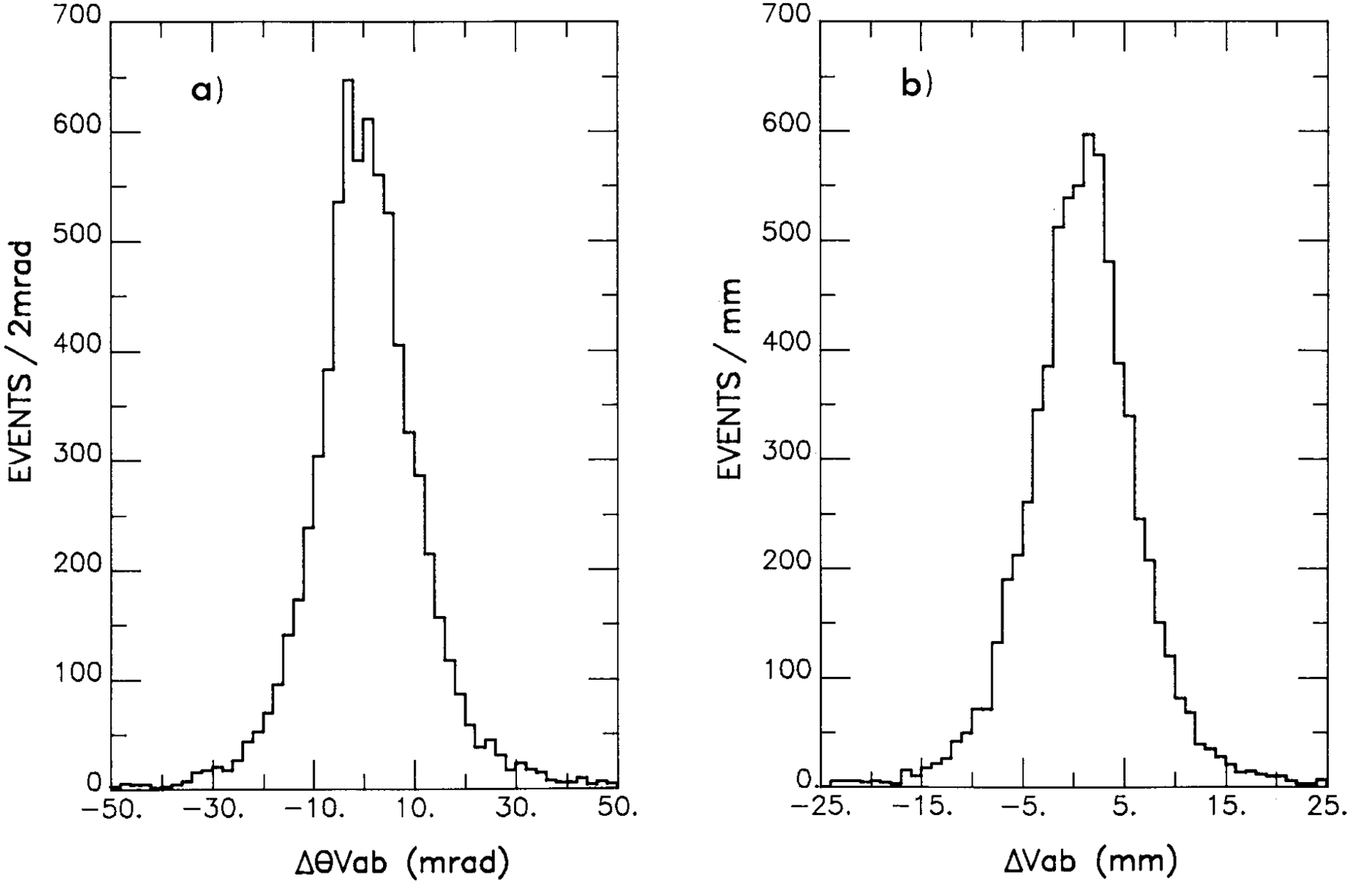
a)
b)
EVENTS / 2mrad
EVENTS / mm
700
600
500
400
300
200
100
0
−50.
−30.
−10.
10.
30.
50.
−25.
−15.
−5.
5.
15.
25.
ΔθVab (mrad)
ΔVab (mm)

Fig. 9

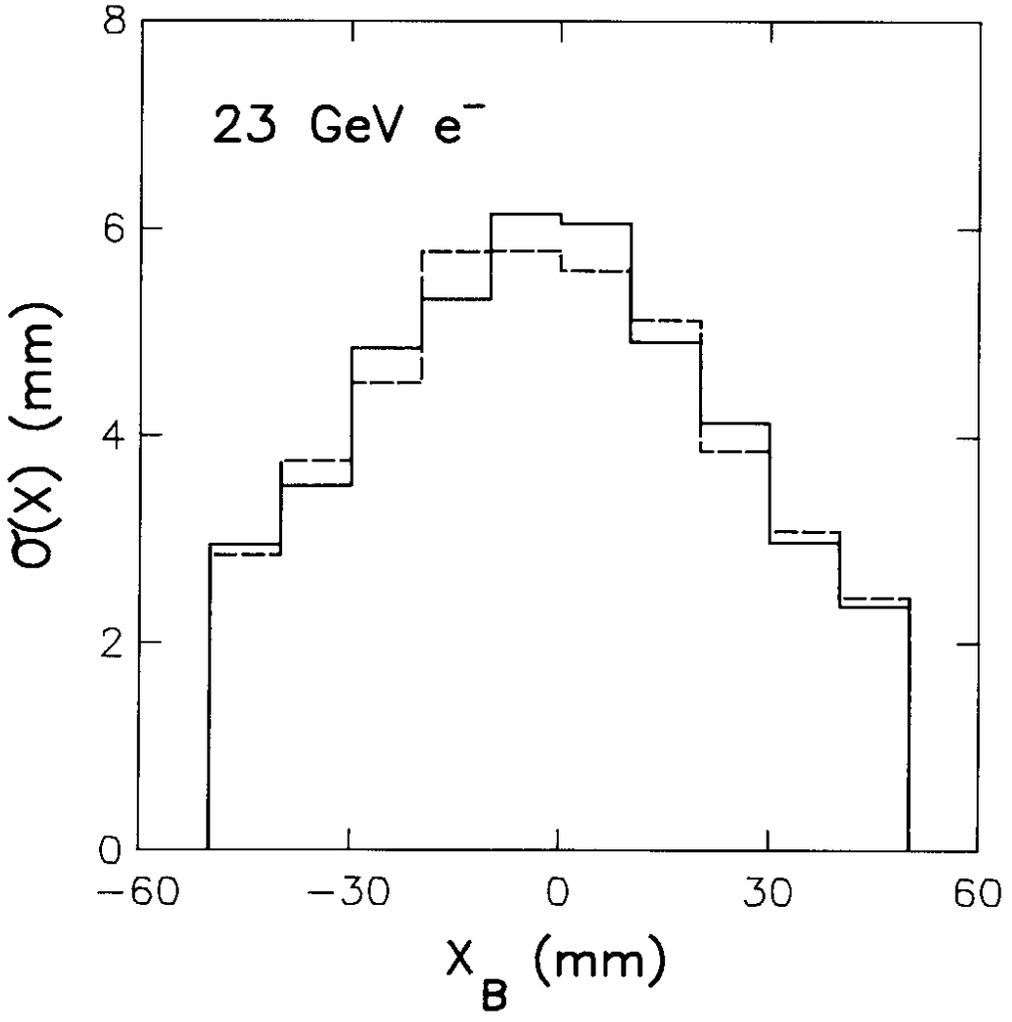

Fig. 10

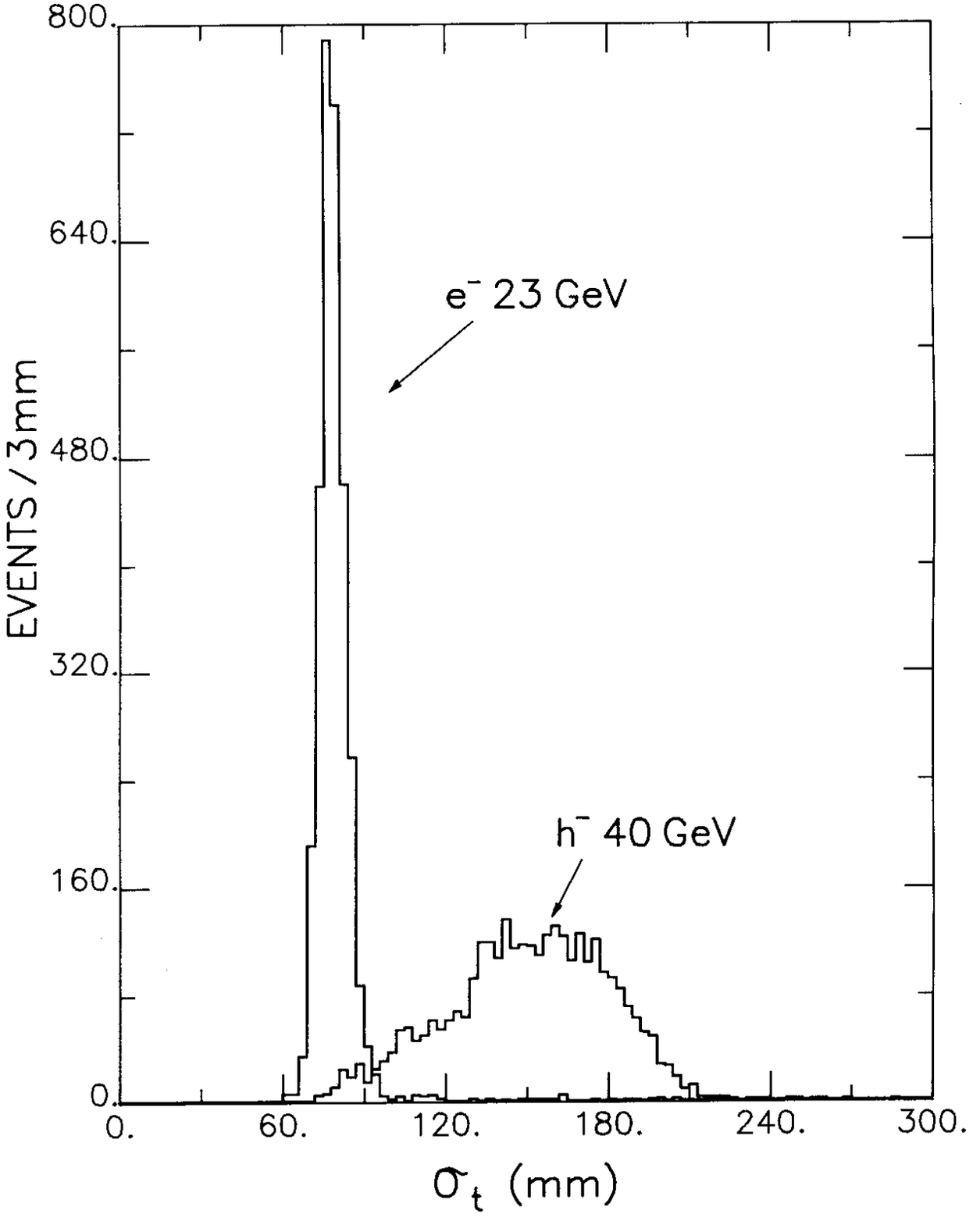
800.
640.
480.
320.
160.
0.
EVENTS / 3mm
e⁻ 23 GeV
h⁻ 40 GeV
0.
60.
120.
180.
240.
300.
σt (mm)

Fig. 11

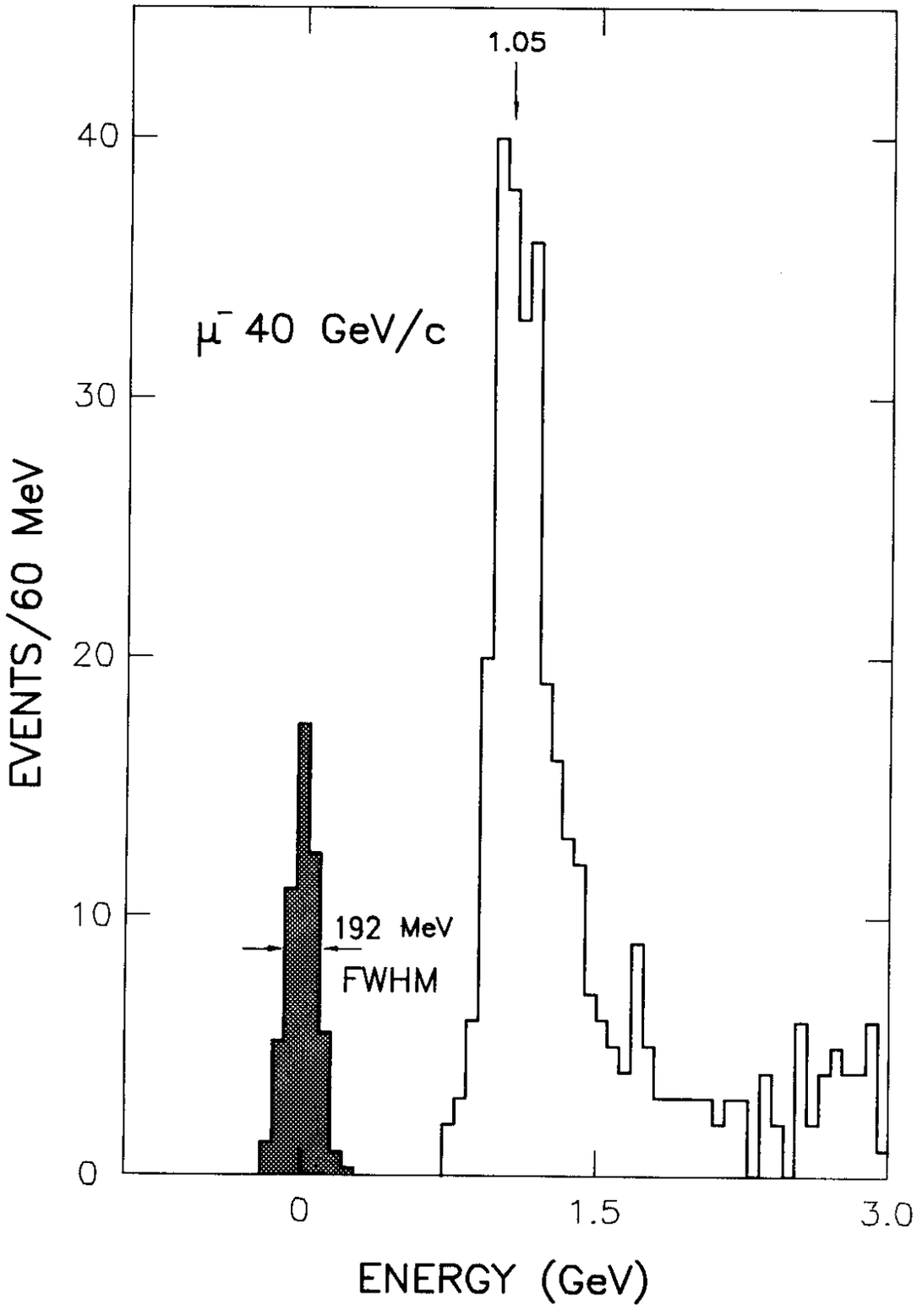
1.05
40
30
20
10
0
μ⁻ 40 GeV/c
EVENTS/60 MeV
192 MeV
FWHM
0
1.5
3.0
ENERGY (GeV)

Fig. 12